Reduced vortex descriptors linking polycrystallinity in magnetic nanoparticles with polarized magnetic small-angle neutron scattering

Michael P. Adams [1,2,*] Jonathan Leliaert [3] Andreas Michels [4] and Elizabeth M. Jefremovas [4,5,†]

[1] *Max Planck Institute for the Structure and Dynamics of Matter, Luruper Chaussee 149, D-22761 Hamburg, Germany*

[2] *Center for Free-Electron Laser Science, Notkestraße 85, D-22607 Hamburg, Germany*

[3] *Department of Solid State Sciences, Ghent University, Krijgslaan 285/S1, 9000 Ghent, Belgium*

[4] *Department of Physics and Materials Science, University of Luxembourg, 162A Avenue de la Faiencerie, L-1511 Luxembourg, Grand Duchy of Luxembourg*

[5] *Institute for Advanced Studies, University of Luxembourg, Campus Belval, L-4365 Esch-sur-Alzette, Grand Duchy of Luxembourg*

(Received 18 August 2026; accepted 23 October 2026; published 5 November 2026)

Analytical vortex models reduce polarized magnetic small-angle neutron scattering (SANS) from nanoparticle ensembles to a small set of texture descriptors. In this work, we apply this reduction to micromagnetic simulations of polycrystalline iron oxide nanoflowers at a fixed particle size and examine how a controlled parametrization of multigrain disorder is reflected in the remanent descriptors. The particles are represented by explicit Voronoi microstructures, and intraparticle disorder is varied through the intergrain exchange coupling and anisotropy-axis coherence. Fitting each remanent magnetization state to a hyperbolic vortex model reveals a predominantly two-channel organization: The intergrain exchange coupling is associated mainly with the radial vortex profile, whereas the anisotropy-axis coherence is associated mainly with the orientational moment of the vortex-axis distribution. The normalized spin-flip SANS cross sections are accurately represented by independent fits of the analytical linear-vortex SANS expression obtained from the first-order expansion of the hyperbolic profile. The fitted orientational descriptor agrees closely with its independent real-space estimate, whereas the corresponding radial descriptors exhibit a strong global nonlinear relation. This separation identifies which information from the micromagnetic vortex textures is robustly retained by the reduced analytical representation.

DOI: 10.1103/mhfg-6sjm

I. INTRODUCTION

Magnetic nanoparticles (MNPs) are often treated within the macrospin approximation as single-domain, uniformly magnetized entities [1]. This description is often adequate for sufficiently small particles (typically tens of nanometers [2–4]), but becomes insufficient in the intermediate-size regime, where microstructural defects and associated magnetic disorder produce complex, nonuniform magnetization textures [5–12].

Multicore iron oxide MNPs (also known as nanoflowers, NFs) constitute a model example of a defect-rich nanoarchitecture. Their excellent macroscopic heat dissipation, key in applications such as magnetic hyperthermia or nanocatalysis [6,13,14], is argued to be a direct consequence of their internal magnetic disorder [11,15–17]. Their complex, nonuniform intraparticle magnetization states result from the interplay among the crystallographic cores, their anisotropy-axis disorder and pinning landscape, and the exchange and dipolar fields. Elucidating the resulting distribution of magnetic moments is therefore essential for connecting their synthesis-controlled structure with their macroscopic magnetic performance.

Polarized small-angle neutron scattering (SANS) is well positioned to address this challenge. This reciprocal-space technique probes statistically averaged nanoscale magnetization correlations in bulk amounts of material [18,19]. It has been used to resolve magnetic correlations in MNP assemblies, including NFs, for which dipolar-coupled moment and supraferromagnetic correlations have been reported [15,20,21]. More recently, nonuniform vortexlike correlations in maghemite multicore aggregates have been studied, illustrating the potential and sensitivity of polarized SANS to elucidate magnetic correlations associated with structural features [22].

This sensitivity also exposes a central ambiguity of the inverse problem: Different real-space magnetization textures or microscopic disorder parameters may produce similar SANS anisotropies. A useful strategy is therefore to combine micromagnetic simulations with analytical vortex models and to reduce the SANS response of vortex-state particles to a small number of collective variables.

Previous works established analytical spin-flip SANS expressions for linear vortex magnetization fields and obtained

*Contact author: michael.adams@mpsd.mpg.de

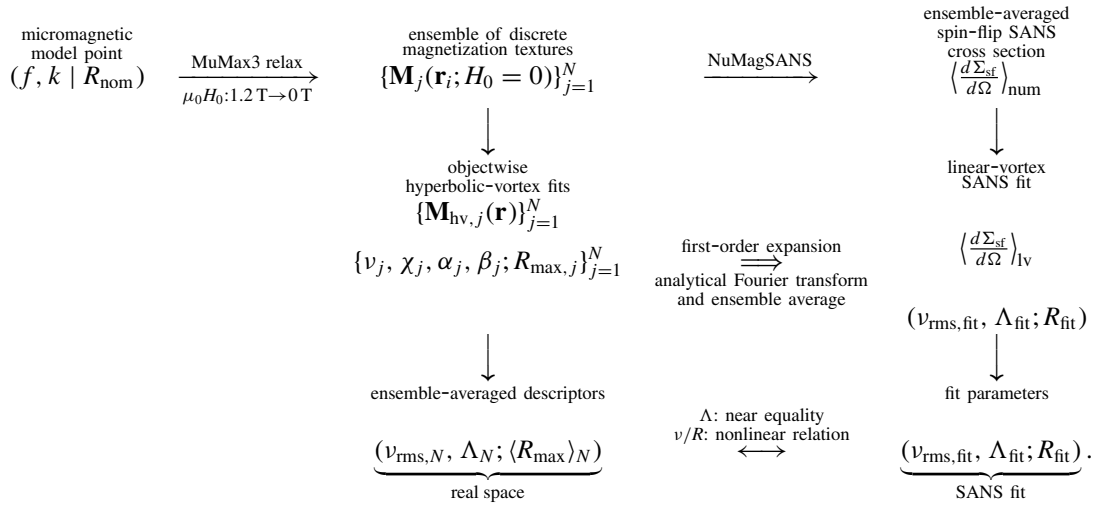
†Contact author: elizabeth.jefremovas@uni.lu

Published by the American Physical Society under the terms of the Creative Commons Attribution 4.0 International license. Further distribution of this work must maintain attribution to the author(s) and the published article's title, journal citation, and DOI. Open access publication funded by Max Planck Society.

the angular anisotropy landscape generated by the radial vortex profile and the vortex-axis distribution [23,24]. A related minimal vortex model showed that the radial profile parameter ν is itself a field-dependent collective coordinate along the hysteresis loop of a spherical, structurally uniform nanoparticle [25]. In those earlier examples, simple axis-distribution models were sufficient to describe the features under consideration. Polycrystalline multicore nanoarchitectures, such as the NFs studied here, introduce two further distinctions within the linear-vortex description: (1) The polar axis distribution enters the spin-flip SANS cross section through the reduced orientational moment Λ and (2) reconstructing the full vortex-axis distribution imposes an additional model assumption. The linear-vortex representation is particularly useful for the reciprocal-space reduction because its polynomial spatial form permits a closed analytical Fourier transform and orientational ensemble average. Thus, the vortex-SANS problem is examined through two complementary reductions. The micromagnetic textures are fitted in real space to obtain radial and orientational vortex descriptors, whereas the numerical SANS cross sections are fitted independently using the analytical linear-vortex expression. Comparing the resulting descriptors tests which information is represented consistently in the real-space and reciprocal-space descriptions.

In this work, we use polycrystalline iron oxide NFs as a forward model for this descriptor-mapping problem. Synthesis studies have demonstrated chemical control over mesocrystal properties, including their size and degree of crystallinity [2,13,26–28]. Here, we represent the resulting magnetic microstructure through a controlled interpolation between random and coherently biased grain-scale anisotropy landscapes, together with a variable intergrain exchange coupling. These parameters define a controlled micromagnetic model rather than direct experimental measures of crystallinity or grain-boundary coupling. Moreover, it has recently been shown that the degree of intraparticle disorder critically affects the macroscopic properties and can promote vortexlike remanent states [11,17], underscoring the importance of microstructural control as a route to tailoring particle functionality. We herein harness such a polycrystalline nanoarchitecture as a model system to evaluate how the controlled multigrain parametrization is reflected in the collective vortex variables that enter the analytical vortex-SANS response.

Our study is therefore deliberately restricted to a controlled remanent configuration: The particles are saturated along $+\mathbf{e}_z$, relaxed, the field is set to zero, and the system is relaxed again (using MuMax3 [29]). At this single field point, we vary two model parameters: (1) the intergrain exchange scale k and (2) the fraction f of grains whose anisotropy axes are aligned with $\mathbf{e}_z$. The resulting numerical and reduced-analysis routes can be summarized as follows:



The two vertical branches represent independent reductions of the same micromagnetic ensemble. The real-space branch fits each magnetization texture objectwise with the hyperbolic vortex model and forms the corresponding ensemble descriptors. The reciprocal-space branch first evaluates the spin-flip SANS cross section directly from the full magnetization fields using the open-source software package NuMagSANS [30] and then fits the resulting numerical pattern with the linear-vortex SANS expression. The double-lined horizontal arrow denotes the analytical model relation: The hyperbolic profile is expanded to first order, Fourier transformed, and ensemble averaged to obtain the linear-vortex SANS expression. It does not denote a direct parameter transfer between the two fits. Their comparison instead reveals which reduced vortex properties are represented consistently in both descriptions. The present work does not attempt a full field-dependent parameter-space screening. Instead, it examines a controlled multigrain micromagnetic model at remanence within the linear-vortex framework.

Section II introduces the micromagnetic model, spin-flip SANS cross section, and analytical vortex reduction; Sec. III presents the resulting collective variables and two-dimensional (2D) SANS patterns; and Sec. IV summarizes the findings. Further details on the simulation and analysis are given in the Supplemental Material [31].

II. METHODS

A. Micromagnetic model

Numerical micromagnetic simulations were performed using MuMax3 [29]. The standard energy contributions consisting of isotropic exchange, (uniaxial) magnetocrystalline anisotropy, dipolar interaction, and Zeeman energy were taken into account. We consider NFs with a nominal diameter of $D_{\mathrm{nom}} = 2R_{\mathrm{nom}} = 100\,\mathrm{nm}$ on a cubic mesh with $36\times36\times36$ cells and a cell-edge length of $a_{\mathrm{cell}} = 5\,\mathrm{nm}$. This discretization is smaller than the exchange length $l_{\mathrm{ex}} = \sqrt{2A/(\mu_0 M_s^2)} \simeq 10.0\,\mathrm{nm}$ of maghemite.

We emphasize that although $a_{\mathrm{cell}} < l_{\mathrm{ex}}$ provides the conventional micromagnetic resolution criterion used here, it does not by itself establish mesh convergence. On a Cartesian finite-difference grid, the curved particle surface and irregular Voronoi boundaries are represented in a staircaselike form, while the discrete exchange operator may introduce an additional grid-dependent anisotropy [32]. The absolute fitted descriptor values may therefore contain a systematic discretization uncertainty that is not quantified in the present work.

The polycrystalline microstructure was generated outside MuMax3 as a fixed three-dimensional (3D) Voronoi region map with a nominal mesocrystal size parameter $g_s = 15\,\mathrm{nm}$ (equivalently, a grain-length scale), and subsequently imported into the micromagnetic simulation. Surface grains were allowed to extend beyond the nominal spherical mask, while nonmagnetic voids inside the nominal sphere were excluded by construction. This procedure fixes the structural ensemble before the micromagnetic calculation and makes the realized grain geometry directly inspectable. The corresponding generation procedure, stored metadata, and validation checks are described in the Supplemental Material [31]. The generated simulation data and the analysis workflow are archived as a Zenodo dataset [33].

Figure 1(a) shows one representative Voronoi realization used as a MuMax3 region map. The actual grain volumes were evaluated directly from the occupied simulation cells, and the volume-derived length $\ell_g = V_g^{1/3}$ was calculated for each grain. The pooled distribution over the simulated NF ensemble is shown in Fig. 1(b). It is approximately described by a Gaussian distribution with a mean of $\mu = 15.28\,\mathrm{nm}$ and a standard deviation of $\sigma = 2.33\,\mathrm{nm}$, consistent with the prescribed structural scale $g_s = 15\,\mathrm{nm}$. The small upward shift reflects the uncut surface grains and the discrete mesh representation. The same metadata define the realized grain- and volume-weighted anisotropy fractions used below, so that both the structural and magnetic disorder are checked before entering the micromagnetic simulations.

To model different degrees of anisotropy-axis coherence, each grain i was assigned a unit anisotropy axis $\mathbf{u}_{\mathrm{ani},i}$. A reference direction $\mathbf{u}_{\mathrm{ani},0} = \mathbf{e}_z$ was defined parallel to the saturating field direction. The dimensionless parameter f denotes the fraction of grains whose anisotropy axes are aligned with this reference direction:

$$f = \frac{N_G^{\parallel}}{N_G}, \tag{1}$$

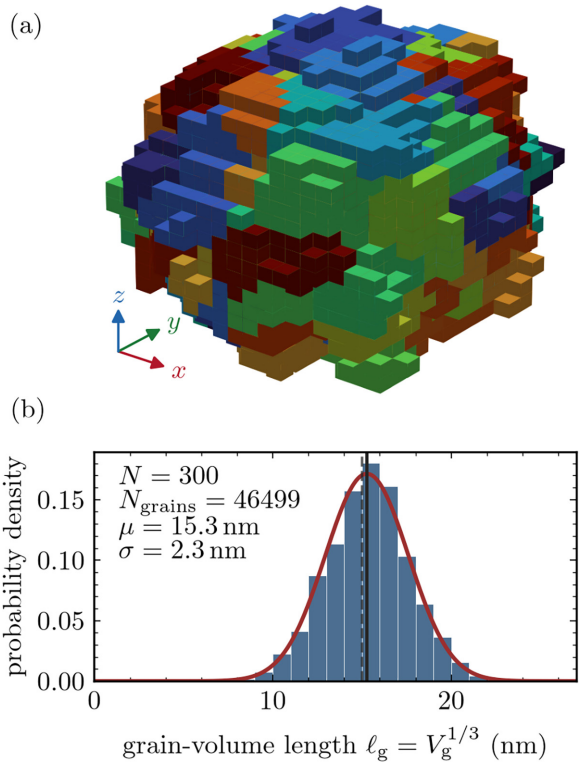


FIG. 1. Example of the micromagnetic nanoflower model. (a) Representative three-dimensional Voronoi realization used to define the polycrystalline grain structure of a single NF. The inset indicates the laboratory axes. (b) Distribution of the volume-derived grain length $\ell_g = V_g^{1/3}$, obtained by pooling the realized grain volumes over the simulated ensemble. The data were obtained for $N = 300$ NFs comprising a total of 46 499 crystallites. The solid curve denotes a Gaussian fit with a mean of $\mu = 15.3\,\mathrm{nm}$ (solid vertical line) and a standard deviation of $\sigma = 2.3\,\mathrm{nm}$. The dashed line indicates the prescribed structural scale $g_s = 15\,\mathrm{nm}$.

where N_G is the number of grains in one NF and $N_G^{\parallel}$ is the number of those grains with $\mathbf{u}_{\mathrm{ani},i} = \mathbf{u}_{\mathrm{ani},0}$. The total number of grains pooled over all $N = 300$ NFs is given only for the ensemble-level histogram in Fig. 1(b). The remaining grains are assigned independent random unit vectors (sampled uniformly on the unit sphere). Consequently, $f = 1$ represents a fully coherent anisotropy-axis configuration, while $f = 0$ represents a random polycrystalline anisotropy-axis distribution. The parameter f is not intended as a direct experimental measure of crystallinity; it is a minimal control parameter for a uniaxial bias in the grain-scale anisotropy landscape. Alternative parametrizations are also possible, such as a continuous axially symmetric distribution of anisotropy axes centered on $\mathbf{e}_z$ with a finite angular width. Such a choice may quantitatively modify the micromagnetic mapping from the disorder parameter to $(\nu_{\mathrm{rms},N}, \Lambda_N)$, while the reduced SANS expression at fixed vortex descriptors remains unchanged within the linear-vortex approximation. The anisotropy assignment is generated independently of the structural geometry by combining a fixed global anisotropy seed with the structural seed of each NF, and ensemble-averaged scattering observables are computed from the resulting set of realizations. The Supplemental Material [31] gives the explicit sampling

procedure, the realized grain- and volume-weighted values of f, and the diagnostics used to exclude unintended correlations with the Voronoi geometry.

Material parameters characteristic of maghemite were taken [11]: saturation magnetization $M_s = 400\,\mathrm{kA/m}$, exchange-stiffness constant $A = 10\,\mathrm{pJ/m}$, and uniaxial anisotropy constant $K_u = 10^4\,\mathrm{J/m^3}$. The intragrain exchange stiffness was kept fixed at A, while the exchange coupling across the grain-boundary regions was rescaled by a dimensionless factor k using the MuMax3 extension "ext_ScaleExchange". Thus, $k = 1$ corresponds to fully exchange-coupled grains, whereas smaller values of k represent weakened intergrain exchange coupling.

For the selected material parameters, the homogeneous defect-free sphere reference estimate for the critical vortex-nucleation radius is $R_{\mathrm{nuc}} = \sqrt{15} l_{\mathrm{ex}} [1 - 6\kappa^2]^{-\frac{1}{2}} \simeq 46.1\,\mathrm{nm}$, with a hardness parameter of $\kappa = \sqrt{K_u/(\mu_0 M_s^2)} \simeq 0.223$ [25,34]. The selected nominal NF radius of $R_{\mathrm{nom}} = 50\,\mathrm{nm}$ is close to this critical radius, with $R_{\mathrm{nom}}/R_{\mathrm{nuc}} \simeq 1.08$. This places the chosen size in a regime that is expected to be particularly sensitive to the competition between broad-core and flux-closure-dominated vortex textures. Because the simulated NFs are polycrystalline, this analytical value serves as a reference scale rather than an exact nucleation threshold. For comparison, the $R_{\mathrm{is}} = 20\,\mathrm{nm}$ iron spheres used for the uniaxial micromagnetic validation of the linear-vortex SANS model in Ref. [23] correspond to $R_{\mathrm{is}}/R_{\mathrm{nuc}} \simeq 2.11$ for their respective material parameters. Those particles were therefore located substantially farther above the analytical nucleation scale than the present NFs, for which $R_{\mathrm{nom}}/R_{\mathrm{nuc}} \simeq 1.08$. The present simulations consequently probe a regime closer to the threshold, although the homogeneous defect-free sphere estimate R_{nuc} remains an approximate reference scale for the polycrystalline NFs.

Unless stated otherwise, the real-space vortex-parameter analysis, structural statistics in Fig. 1(b), and the direct NuMagSANS [30] ensemble averages in Fig. 5(a) use the simulated parameter grid $f = \{0, 0.1, \ldots, 1.0\}$ and $k = \{0.1, 0.25, 0.5, 0.7, 1.0\}$, with $N = 300$ independently generated NFs for each parameter pair. The best-fit reduced analytical patterns in Fig. 5(b) are obtained independently from the normalized NuMagSANS cross sections, while Figs. 5(c) and 5(d) compare the fitted parameters with the corresponding $N = 300$ real-space vortex descriptors. The ensemble is dilute in the sense that each NF is simulated independently; interparticle dipolar correlations are outside the scope of the present forward model. Here, k and f are micromagnetic model parameters; their relation to synthesis-controlled grain-boundary coupling or crystallinity is therefore model dependent.

All states analyzed in this work were generated using the same field protocol. The magnetization was initialized uniformly along the $+\mathbf{e}_z$ direction. A saturating field of $\mu_0 H_0 = 1.2\,\mathrm{T}$ was then applied along $+\mathbf{e}_z$, and the system was relaxed. After this high-field relaxation, the external field was set to $\mu_0 H_0 = 0\,\mathrm{T}$, followed by a second relaxation. The analyzed configuration is therefore a remanent state defined by this two-step field protocol, not a field-following state sampled along a complete hysteresis loop. This distinction is important because the radial vortex profile is in general field dependent [25]. In the present work, we therefore examine how the selected polycrystalline parametrization is reflected in the remanent radial profile and vortex-axis distribution at this single field point. The energy functional, intergrain exchange scaling, and file-indexing protocol are summarized in the Supplemental Material [31].

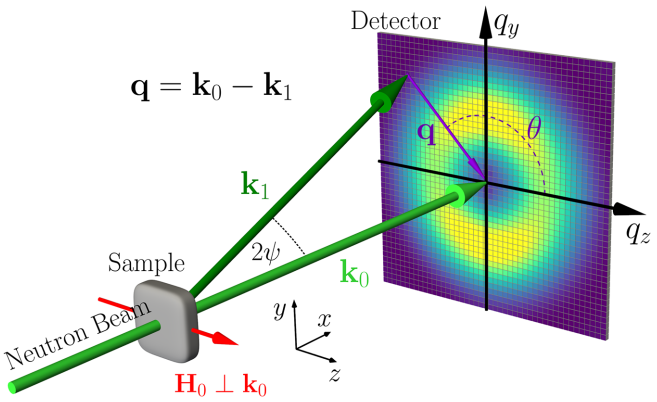


FIG. 2. Scattering geometry used throughout this work. The applied magnetic (guide) field $\mathbf{H}_0 \parallel \mathbf{e}_z$ is perpendicular to the incident neutron wave vector $\mathbf{k}_0 \parallel \mathbf{e}_x$, and the scattering vector $\mathbf{q} = \mathbf{k}_0 - \mathbf{k}_1$ is detected in the (q_y, q_z) detector plane. The azimuthal detector angle θ is measured with respect to the field direction.

B. Spin-flip SANS cross section

The results for the spin-flip SANS cross section are calculated for the scattering geometry where the applied magnetic (guide) field $\mathbf{H}_0 \parallel \mathbf{e}_z$ is perpendicular to the incident neutron beam ($\mathbf{k}_0 \parallel \mathbf{e}_x$), as sketched in Fig. 2. This configuration is commonly employed in uniaxial polarization analysis experiments. The corresponding elastic differential spin-flip SANS cross section $d\Sigma_{\mathrm{sf}}/d\Omega$ reads [19]

$$\frac{d\Sigma_{\mathrm{sf}}}{d\Omega} = \frac{8\pi^3}{V} b_{\mathrm{H}}^2 [|\widetilde{M}_x|^2 + |\widetilde{M}_y|^2 \cos^4\theta + |\widetilde{M}_z|^2 \sin^2\theta \cos^2\theta - (\widetilde{M}_y \widetilde{M}_z^* + \widetilde{M}_y^* \widetilde{M}_z) \sin\theta \cos^3\theta], \quad (2)$$

where V is the scattering volume, $b_{\mathrm{H}} = 2.91 \times 10^8\,\mathrm{A^{-1}\,m^{-1}}$ is the magnetic scattering length in the small-angle regime (the atomic magnetic form factor is approximated by 1, since we are dealing with forward scattering), $\widetilde{\mathbf{M}}(\mathbf{q}) = \{\widetilde{M}_x, \widetilde{M}_y, \widetilde{M}_z\}$ denotes the Fourier transform of the magnetization vector field $\mathbf{M}(\mathbf{r}) = \{M_x, M_y, M_z\}$, θ is the angle between $\mathbf{H}_0 = H_0 \mathbf{e}_z$ and $\mathbf{q}$, so that $\mathbf{q} \simeq q\{0, \sin\theta, \cos\theta\}$ in small-angle approximation, and the asterisks "$*$" mark the complex conjugate. Note that the polarization-dependent chiral function has been neglected in Eq. (2) because the experimentally accessible spin-flip sum corresponds to the average of the two spin-flip channels and thereby removes the antisymmetric chiral contribution. Independent of this formal cancellation in the summed channel, the simulated ensembles are also close to balanced in chirality: For each (f, k) case, the fraction with $\chi = +1$ lies between 0.44 and 0.56 for $N = 300$ NFs.

The Fourier components $\widetilde{M}_{x,y,z}(\mathbf{q})$ are numerically computed from the results $M_{x,y,z}(\mathbf{r})$ of the micromagnetic (real-space) simulations using the NuMagSANS software package

[30]. The 2D spin-flip SANS cross section [Eq. (2)] depends on q_y and q_z, or equivalently on $q = (q_y^2 + q_z^2)^{1/2}$ and $\theta = \arctan2(q_y, q_z)$. These direct numerical evaluations provide the reference SANS landscape in Fig. 5(a). Note that vortex-vortex interparticle dipolar interactions are not included in the present forward model; the analysis is restricted to dilute ensembles of independently simulated NFs.

C. Analytical vortex model

The interpretation of the micromagnetic textures is guided by the analytical vortex-SANS framework introduced for individual vortex particles in Ref. [23] and by the corresponding angular anisotropy landscape of vortex ensembles developed in Ref. [24]. Both studies provide the reduced language used here: In the leading linear-vortex projection, the spin-flip SANS response of vortex-state particles is organized by the radial vortex profile and by the distribution of vortex-axis orientations. Our micromagnetic analysis therefore does not start from the full 3D magnetization field alone, but first projects each simulated state onto collective variables used in the analytical vortex-SANS theory.

For each simulated remanent state $\mathbf{M}(\mathbf{r}; H_0 = 0)$, the vortex parameter $\nu \geqslant 0$, the chirality $\chi = \pm 1$, the polar angle α, and the azimuthal angle β were extracted by fitting (detailed in the Supplemental Material [31]) the rotated analytical hyperbolic vortex magnetization vector field:

$$\mathbf{M}_{\mathrm{hv}}(\mathbf{r}) = \mathbf{R}(\alpha, \beta)\mathbf{M}'_{\mathrm{hv}}(\mathbf{R}^T(\alpha, \beta)\mathbf{r}),$$
$$\mathbf{M}'_{\mathrm{hv}}(\mathbf{r}') = M_{\mathrm{s}}\,\mathrm{sech}\left(\nu\frac{\rho'}{R}\right)\mathbf{e}_{z'} + \chi M_{\mathrm{s}}\tanh\left(\nu\frac{\rho'}{R}\right)\mathbf{e}_{\phi'}, \quad (3)$$

where $\mathbf{R} = \mathbf{R}_z(\beta)\mathbf{R}_y(\alpha)$ is the rotation matrix, R is the particle radius, $\rho' = \sqrt{(x')^2 + (y')^2}$ is the radial cylinder coordinate, $\mathbf{e}_{\phi'} = \{-y'/\rho', +x'/\rho', 0\}$ is the azimuthal unit vector, and M_{s} is the saturation magnetization. Here, the primed coordinates, e.g., $\mathbf{r}'$, denote the local coordinates, whereas the unprimed coordinates refer to the global coordinates. The parameter ν controls the radial vortex profile: A larger ν corresponds to a narrower vortex core, a smaller ν to a broader vortex core, and $\nu = 0$ to a uniform magnetization state. Because $N = 300$ NFs were simulated for each (f, k) pair, the fitting procedure yielded $N = 300$ corresponding parameter sets $(\nu, \chi, \alpha, \beta)$.

The functional form of the fitted hyperbolic profile is connected to the closed analytical SANS expressions of Refs. [23,24] through the corresponding linear-vortex approximation. It is obtained as the small-ρ'/R limit of Eq. (3),

$$\mathbf{M}_{\mathrm{lv}}(\mathbf{r}) = \mathbf{R}(\alpha, \beta)\mathbf{M}'_{\mathrm{lv}}(\mathbf{R}^T(\alpha, \beta)\mathbf{r}),$$
$$\mathbf{M}'_{\mathrm{lv}}(\mathbf{r}') = M_{\mathrm{s}}\mathbf{e}_{z'} + M_{\mathrm{s}}\chi\nu\frac{\rho'}{R}\mathbf{e}_{\phi'}. \quad (4)$$

Within the linear-vortex representation, ν fixes the relative weight of the circulating contribution. The purpose of this projection is not to approximate the complete hyperbolic texture pointwise throughout the particle. Rather, it maps the leading vortex symmetry onto a magnetization field that is polynomial in the spatial coordinates, so that its Fourier transform and orientational ensemble average remain analytically closed. At the level of the local small-ρ'/R expansion, ν/R is the first-order radial slope. The independently optimized real-space and reciprocal-space radial parameters used below, however, solve different global projection problems and therefore need not coincide numerically.

Following the notation of Refs. [23,24], with $u = qR$, $F(u) = (\sin u - u\cos u)/u^3$, and $W = 3V_{\mathrm{s}}^2 b_{\mathrm{H}}^2 M_{\mathrm{s}}^2/V$, the resulting $(\nu, \chi, \alpha, \beta)$-ensemble-averaged spin-flip SANS cross section is (details in the Supplemental Material [31])

$$\left\langle\frac{d\Sigma_{\mathrm{sf}}}{d\Omega}\right\rangle_{\mathrm{lv}} = \frac{W}{8}[F(qR)]^2\mathcal{A}_0(\theta) + \frac{W}{2}\nu_{\mathrm{rms}}^2[F'(qR)]^2\mathcal{A}_1(\theta), \quad (5)$$

where the angular profile functions are defined as

$$\mathcal{A}_0(\theta) = 12 - \Lambda(3\cos^2 2\theta + 2\cos 2\theta + 3) + 4\cos 2\theta,$$
$$\mathcal{A}_1(\theta) = 3 - (2\Lambda - 1)\cos 2\theta. \quad (6)$$

For the ensemble average in Eq. (5), the variables $(\nu, \chi, \alpha, \beta)$ are assumed to be statistically independent. In addition, we assume a monodisperse particle radius R, equal probabilities for the two circulation senses, and a uniform distribution of β on the interval $[0, 2\pi)$. The remaining polar-axis distribution is described by the α-dependent density $\psi_\alpha(\alpha)$, normalized according to $\int_0^\pi \psi_\alpha(\alpha)\sin\alpha\, d\alpha = 1$. In contrast to Refs. [23,24], where Eq. (5) was evaluated for a prescribed angular probability density $\psi(\alpha, \beta)$, we do not impose a specific parametric form on the polar distribution in the main analysis. Instead, its contribution is expressed through the orientational moment:

$$\Lambda = 3\langle\cos^2\alpha\rangle - 1, \quad (7)$$

where the average is explicitly defined as

$$\langle\cos^2\alpha\rangle = \int_0^\pi \psi_\alpha(\alpha)\cos^2\alpha\,\sin\alpha\, d\alpha. \quad (8)$$

Given that $0 \leqslant \langle\cos^2\alpha\rangle \leqslant 1$, the orientational moment is bounded by $-1 \leqslant \Lambda \leqslant 2$. The lower bound corresponds to a purely transverse axis distribution, $\psi_\alpha(\alpha) = \delta(\alpha - \pi/2)$, yielding $\Lambda = -1$. The upper bound is reached when all orientational weight is concentrated at $\alpha = 0$ and/or $\alpha = \pi$, yielding $\Lambda = 2$. In contrast, $\Lambda = 0$ is obtained both for an isotropic distribution, $\psi_\alpha(\alpha) = 1/2$, and for a uniform distribution restricted to either the northern or southern hemisphere. Thus, distinct polar-axis distributions can have the same value of Λ, because this moment does not uniquely determine $\psi_\alpha(\alpha)$. For the finite micromagnetic ensemble, the corresponding empirical moment is estimated directly from the extracted polar angles as

$$\Lambda_N = \frac{1}{N}\sum_{j=1}^{N}(3\cos^2\alpha_j - 1), \quad (9)$$

where α_j is the fitted polar vortex-axis angle of the jth NF. The Supplemental Material compares the empirical polar distributions $\psi_\alpha(\alpha)$ with uniform-band and linear-segment representations [31]. Their limited accuracy for some parameter combinations motivates the direct use of Λ in the main analysis, without imposing a specific functional form for $\psi_\alpha(\alpha)$.

In the linear-vortex expression, the radial parameter enters the spin-flip SANS cross section quadratically. We therefore

summarize the independently fitted real-space values ν_j by the empirical root-mean-square value $\nu_{\mathrm{rms},N}$:

$$\nu_{\mathrm{rms},N}^2 = \langle \nu^2 \rangle_N = \frac{1}{N} \sum_{j=1}^{N} \nu_j^2. \tag{10}$$

This quantity is the real-space radial descriptor corresponding to the quadratic radial coefficient in the reduced SANS model; it is used below as a reference quantity and is not inserted into the independent SANS fits. For the real-space fit of the jth NF, R is set to the object-specific maximum radial extent $R_{\mathrm{max},j}$, as defined in the Supplemental Material [31]. This choice defines an object-specific enclosing scale that contains all retained magnetic-cell centers and fixes the radial normalization of the hyperbolic-vortex fit. Thus, $R_{\mathrm{max},j}$ is a normalization scale rather than an independently fitted particle or scattering radius; the realized irregular NF mask remains unchanged during the fit. For the comparison in Fig. 5(c), we use the arithmetic ensemble mean $\langle R_{\mathrm{max}} \rangle_N = N^{-1} \sum_{j=1}^{N} R_{\mathrm{max},j} = 62.79\,\mathrm{nm}$. This value exceeds the nominal radius $R_{\mathrm{nom}} = 50\,\mathrm{nm}$ by approximately 12.8 nm, which is comparable to the prescribed grain-length scale $g_s = 15\,\mathrm{nm}$. The excess maximum extent arises because the surface Voronoi grains are retained without truncation at the nominal spherical boundary. In contrast, the realized magnetic volumes correspond to a mean volume-equivalent radius of 52.06 nm, with a standard deviation of 0.25 nm.

Figure 3 illustrates the real-space reduction for one representative parameter combination. The agreement of $m_{\phi'}$ and $m_{z'}$ with Eq. (3) shows that the fitted hyperbolic model captures the dominant radial structure of the simulated vortexlike textures. Equation (5) provides the analytical basis for the best-fit SANS representations in Fig. 5(b). The independently extracted real-space descriptors $\nu_{\mathrm{rms},N}$ and Λ_N provide the reference quantities for the comparisons in Figs. 5(c) and 5(d). The following section examines how these two descriptors depend on the NF parameters k and f.

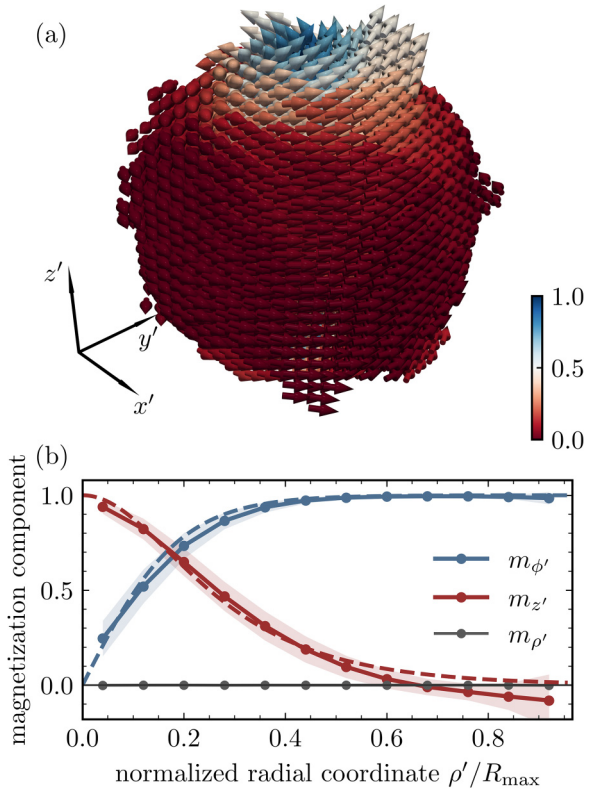


FIG. 3. Real-space vortex characterization for a representative remanent NF ensemble with $f = 0.4$, $k = 0.25$, and $N = 300$. (a) Three-dimensional magnetization vector field of a representative NF after transformation into the fitted vortex-axis coordinate system; color bar encodes the $m_{z'}$ component. (b) Ensemble-averaged radial profiles in the same coordinate system. Symbols denote the mean binned micromagnetic profiles, and shaded bands denote three standard deviations across the ensemble for $m_{\phi'}$ and $m_{z'}$. Averaged over the radial bins, the corresponding 3σ half-widths are 0.033 and 0.066, respectively. Dashed lines show the hyperbolic vortex model [Eq. (3)] evaluated with $\nu_{\mathrm{rms},N} = 5.26$; the fitted individual values have a standard deviation of 0.20.

III. RESULTS AND DISCUSSION

A. Collective variables

We first analyze the radial vortex profile through $\nu_{\mathrm{rms},N} = \sqrt{\langle \nu^2 \rangle_N}$, where ν is fitted for each NF from Eq. (3). We then summarize the vortex-axis distribution by the empirical moment Λ_N defined in Eq. (9). Both quantities are evaluated for each simulated pair of micromagnetic parameters (k, f).

Figure 4 shows that the two extracted descriptors respond differently to the two micromagnetic control parameters (k, f). The ensemble root-mean-square radial vortex-profile parameter $\nu_{\mathrm{rms},N}$ decreases with increasing intergrain exchange scale k, which corresponds to an increasing vortex-core broadening, and follows roughly an exponential decay with k. Its dependence on f is weaker over the sampled parameter range. Qualitatively, reducing k weakens exchange-driven alignment across the grain boundaries relative to the magnetostatic tendency toward flux closure, consistent with the narrower fitted vortex cores at small k. In contrast, the orientational moment Λ_N varies primarily with f. For $k = 0.1$–0.7, increasing the fraction f of grains with $\mathbf{u}_{\mathrm{ani},i} = \mathbf{u}_{\mathrm{ani},0}$ drives Λ_N from positive values, corresponding to axes biased toward the field direction, to values close to -1, corresponding to predominantly transverse vortex axes for $f \gtrsim 0.5$. The $k = 1$ curve is displaced from this collapse, indicating that very strong intergrain exchange partially suppresses the transverse locking of the vortex axes. For the fixed, near-threshold particle size considered here, a qualitative interpretation is that a vortex axis transverse to $\mathbf{e}_z$ allows part of the circulating magnetization to acquire components along the coherent easy-axis direction, whereas a field-parallel vortex has its circulating component mainly perpendicular to $\mathbf{e}_z$. The observed vortex-axis reorientation may therefore reflect competition among coherent uniaxial anisotropy, exchange, and dipolar energy in the remanent state, rather than a purely geometrical effect.

The positive-Λ_N region also connects directly to the uniaxial iron-sphere simulations reported in Ref. [23]. These simulations followed the major hysteresis loop from magnetic saturation through remanence. Within the analytical cone model used in Ref. [23], the high-field limit is described by

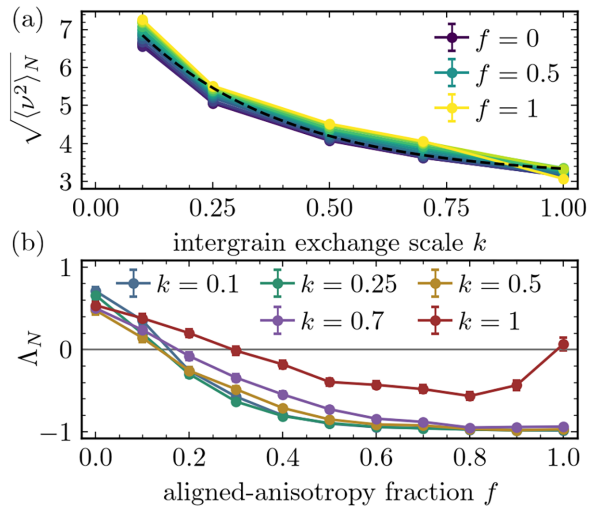


FIG. 4. Collective vortex descriptors extracted directly from the remanent micromagnetic states. (a) Root-mean-square ensemble value $\nu_{\mathrm{rms},N} = \sqrt{\langle \nu^2 \rangle_N}$ [Eq. (10)] of the fitted radial vortex-profile parameter as a function of intergrain exchange scale k. Colors denote different aligned-anisotropy fractions f, and the dashed line shows a common $x_1 + x_2 \exp(-x_3 k)$ fit to all points. (b) Empirical orientational moment Λ_N [Eq. (9)], computed directly from the fitted vortex axes for each (f, k). Positive Λ_N denotes axes biased toward the field direction, while negative Λ_N denotes predominantly transverse vortex axes.

a vanishing vortex amplitude ν and $\alpha_c \to 0^\circ$, whereas the vortex-axis distribution broadens as the field is reduced. At remanence, the vortex-axis ensemble obtained for uniaxial anisotropy was represented by a uniform spherical-cap distribution with $\alpha_c = 54^\circ$. For this distribution, the orientational moment is

$$\Lambda = \cos\alpha_c + \cos^2\alpha_c \simeq 0.93, \tag{11}$$

corresponding to a pronounced field bias and a vertical twofold spin-flip SANS anisotropy.

More generally, for a uniform spherical-cap distribution defined by $0 \leqslant \alpha \leqslant \alpha_c$, the orientational moment is given by the same expression. Even when α_c is formally extended over the full interval $0 \leqslant \alpha_c \leqslant \pi$, this parametrization is restricted to

$$-\tfrac{1}{4} \leqslant \Lambda \leqslant 2, \tag{12}$$

with its minimum reached at $\alpha_c = 2\pi/3$. The spherical-cap model therefore cannot represent the strongly transverse regime with $\Lambda_N \simeq -1$ found in the present simulations. The direct use of the empirical orientational moment Λ_N removes this restriction without imposing a specific functional form on the vortex-axis distribution.

Formally, $\alpha_c \to 0^\circ$ corresponds to $\Lambda \to 2$. At complete saturation, however, the vortex amplitude ν vanishes and the vortex axis is no longer an independent physical degree of freedom. Together with the field dependence of the radial vortex-profile parameter demonstrated using the hyperbolic vortex model in Ref. [25], this shows that both reduced descriptors can evolve along the magnetic-field cycle. The present parameter grid contains the field-biased remanent regime at small f and weak intergrain exchange, but additionally extends into the predominantly transverse regime with $\Lambda_N \simeq -1$.

Thus, in this remanent protocol, k is mainly associated with the radial vortex-profile channel, whereas f is mainly associated with the vortex-orientation channel. This separation is not an assumed property of the model, but an outcome of the present micromagnetic ensemble. It motivates the use of $\nu_{\mathrm{rms},N}$ and Λ_N as real-space reference descriptors for comparison with the effective parameters obtained from the normalized SANS fits.

The Supplemental Material [31] gives the complete $\psi_\alpha(\alpha)$ grids and compares uniform-band and linear-segment representations. These compact distributions are useful for visualizing the axis statistics, but some parameter points are not faithfully represented by such simple densities. The main-text analysis therefore uses Λ_N as the empirical real-space orientational descriptor and compares it directly with Λ_{fit}, while the detailed $\psi_\alpha(\alpha)$ modeling is retained as a diagnostic layer.

B. Two-dimensional spin-flip SANS

Figure 5 compares the numerical spin-flip SANS cross sections calculated from the micromagnetic magnetization fields using NuMagSANS [30] [Fig. 5(a)] with the corresponding best fits of the linear-vortex SANS model [Fig. 5(b)]. For each (f, k), the parameters $\nu_{\mathrm{rms,fit}}$, Λ_{fit}, and R_{fit} were obtained by minimizing the pixelwise error between the individually normalized numerical and analytical cross sections. Consequently, the comparison tests the ability of the linear-vortex model to represent the radial and angular pattern shape, but neither its absolute intensity nor a parameter-free forward prediction from the real-space descriptors. The mean normalized root-mean-square error (RMSE) is 0.0124.

The radial scales extracted from the SANS and real-space analyses show a strong global nonlinear relation [Fig. 5(c)], whereas Λ_{fit} closely follows the real-space moment Λ_N [Fig. 5(d)]. This orientational agreement is nontrivial because the numerical cross sections originate from the full irregular micromagnetic textures rather than from the reduced linear-vortex model. Nevertheless, Λ_{fit} follows Λ_N with a Pearson correlation coefficient of 0.998 and an RMSE of 0.0368, despite the moderate deviations from the factorization assumption documented in the Supplemental Material [31]. The nonlinear relation in Fig. 5(c) represents a global empirical trend over all sampled (f, k) combinations. It is not assumed to hold separately along fixed-f or fixed-k subsets and therefore does not define a unique pointwise conversion between the real-space and SANS-fit radial descriptors. The fitted radii are narrowly distributed around the nominal NF radius, with $\langle R_{\mathrm{fit}} \rangle = 49.93\,\mathrm{nm}$ and $\sigma_R = 0.51\,\mathrm{nm}$ [Fig. 5(e)]. We note that, in contrast to $R_{\max}$, which fixes the enclosing normalization scale of each real-space fit, R_{fit} is inferred from the radial q dependence of the ensemble-averaged SANS pattern and therefore represents an effective spectral radius rather than the outermost extent of the individual NFs. The underlying real-space vortex-axis distributions and additional comparisons with explicit models for $\psi_\alpha(\alpha)$ are documented in the Supplemental Material [31].

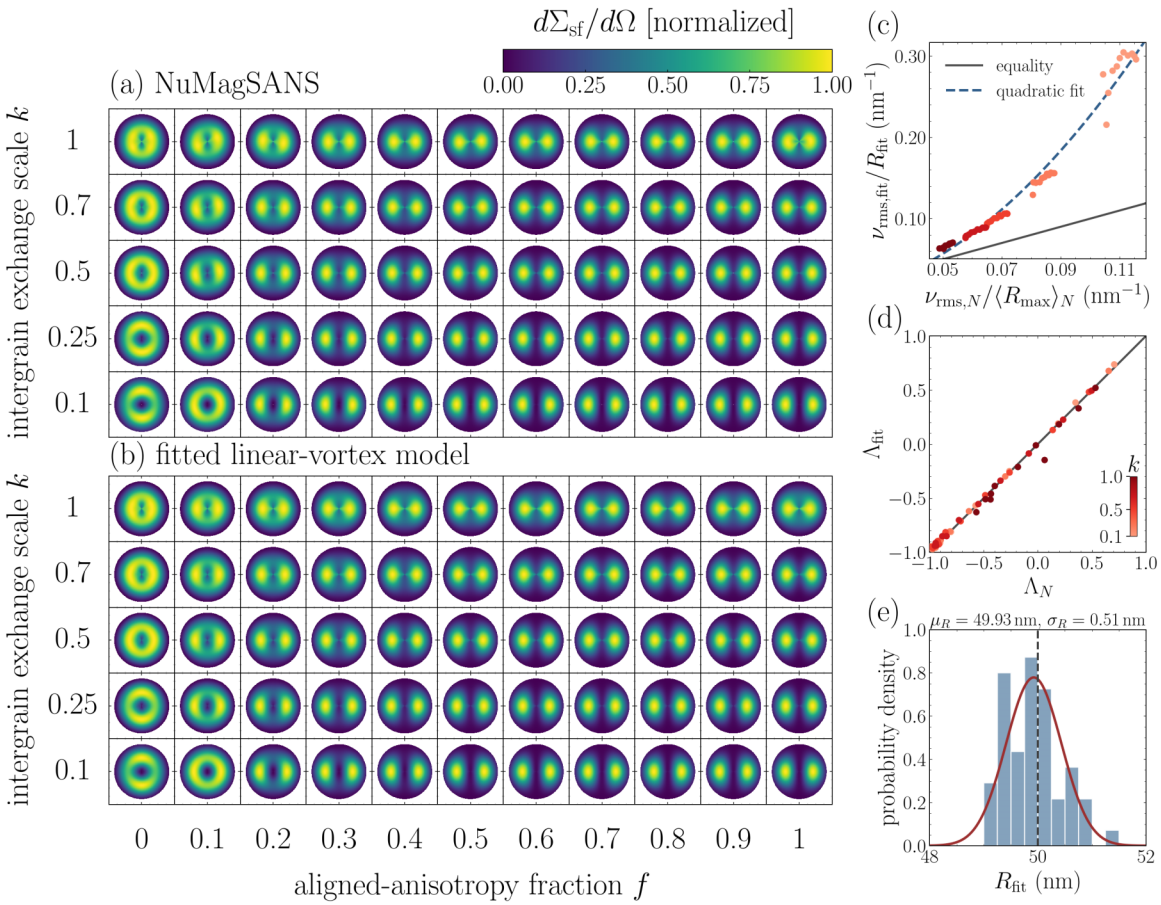


FIG. 5. Comparison of the numerical and reduced analytical 2D spin-flip SANS landscapes at remanence. The applied magnetic field $\mathbf{H}_0$ is horizontal in the plane, where the horizontal coordinate is q_z and the vertical one is q_y. (a) NuMagSANS cross sections [30] computed from the micromagnetic magnetization fields of $N = 300$ independently generated NFs. (b) Best-fit linear-vortex SANS cross sections obtained independently for each (f, k) using $\nu_{rms,fit}$, Λ_{fit}, and R_{fit}. The horizontal grid axis gives the fraction f of grains with $\mathbf{u}_{ani,i} = \mathbf{u}_{ani,0}$, while the vertical grid axis gives the intergrain exchange scale k. The patterns in panels (a) and (b) are displayed for $q \leqslant 0.10\,\mathrm{nm}^{-1}$, corresponding to $qR \leqslant 5$ for the nominal radius of $R_{nom} = 50\,\mathrm{nm}$, and are normalized separately to compare their shapes rather than absolute intensities. (c) Comparison of the real-space radial inverse scale $\nu_{rms,N}/\langle R_{max}\rangle_N$ with the SANS-fit radial inverse scale $\nu_{rms,fit}/R_{fit}$; the solid line denotes equality and the dashed line the global quadratic fit. (d) Comparison of Λ_{fit} with the empirical real-space moment Λ_N; the line denotes equality and colors indicate k. (e) Distribution of R_{fit} with a Gaussian fit.

The radial evolution of the numerical SANS cross sections can be summarized by azimuthal averaging,

$$I(q) = \frac{1}{2\pi}\int_0^{2\pi}\left\langle \frac{d\Sigma_{sf}}{d\Omega}\right\rangle(q,\theta)\,d\theta. \tag{13}$$

For each (f, k), the peak position q_{max}, peak intensity I_{max}, and relative central intensity $I(0)/I_{max}$ are extracted from this radial average. Table I compares their averages over the sampled values of f with the corresponding real-space descriptor $\langle\nu_{rms,N}\rangle_f$. With increasing k, $\langle\nu_{rms,N}\rangle_f$ decreases from 6.915 to 3.220, while $\langle q_{max}R_{nom}\rangle_f$ decreases from 2.462 to 1.924 and $\langle I(0)/I_{max}\rangle_f$ increases from 0.059 to 0.724. As shown in Fig. 4, the variation over f is small compared with this systematic dependence on k. For weak intergrain exchange, $\langle q_{max}R_{nom}\rangle_f = 2.462$ lies close to the maximum of $|F'(qR)|$ at $qR \simeq 2.5$ in the linear-vortex model. Increasing k shifts the numerical maximum toward smaller q and raises the relative central intensity, consistent with the vortex-core broadening indicated by the decreasing radial descriptor in Fig. 4(a). The evolution of the angular anisotropy can be interpreted through the angular factors $\mathcal{A}_0(\theta)$ and $\mathcal{A}_1(\theta)$ in Eq. (6). We therefore consider three characteristic parameter regions separately.

In the following limiting-case discussion, the values of $\nu_{rms,N}$ and Λ_N from Fig. 4 are used to locate the different (f, k) regions and to characterize their real-space vortex profiles qualitatively. The generic parameter ν_{rms} appearing in the analytical expressions below denotes the radial coefficient of

TABLE I. Comparison of the real-space radial vortex descriptor with radial characteristics of the azimuthally averaged numerical spin-flip SANS cross sections. The brackets denote averages over the sampled values of f, and $I_{max} = \max_q I(q)$.

k	$\langle\nu_{rms,N}\rangle_f$	$\langle q_{max}R_{nom}\rangle_f$	$\langle I(0)/I_{max}\rangle_f$
0.10	6.915	2.462	0.059
0.25	5.293	2.377	0.212
0.50	4.289	2.238	0.427
0.70	3.822	2.123	0.561
1.00	3.220	1.924	0.724

the linear-vortex SANS model and is not identified point by point with the real-space estimator $\nu_{\mathrm{rms},N}$.

a. Parameter region $f \gtrsim 0.5$, $0.1 \lesssim k \lesssim 0.7$. As shown in Fig. 4, for $f \gtrsim 0.5$ and $0.1 \lesssim k \lesssim 0.7$, the orientational moment approaches $\Lambda_N \simeq -1$, indicating a predominantly transverse vortex-axis distribution. Within this parameter region, the radial vortex descriptor lies approximately in the interval $4 \lesssim \nu_{\mathrm{rms},N} \lesssim 7$. For the limiting case $\Lambda = -1$, the analytical SANS cross section (5) has the finite Fourier representation:

$$\left\langle \frac{d\Sigma_{\mathrm{sf}}}{d\Omega} \right\rangle_{\Lambda=-1} = I_0(q) + I_2(q)\cos 2\theta + I_4(q)\cos 4\theta, \quad (14)$$

with the q-dependent intensities (for $\Lambda = -1$):

$$I_0(q) = \frac{3W}{2}\left[\frac{11}{8}[F(qR)]^2 + \nu_{\mathrm{rms}}^2[F'(qR)]^2\right],$$
$$I_2(q) = \frac{3W}{2}\left[\frac{1}{2}[F(qR)]^2 + \nu_{\mathrm{rms}}^2[F'(qR)]^2\right],$$
$$I_4(q) = \frac{3W}{16}[F(qR)]^2. \quad (15)$$

At $\theta = \{0,\ \pi\}$, the second-order harmonic yields $\cos 2\theta = 1$, whereas at $\theta = \{\pi/2,\ 3\pi/2\}$ it is $\cos 2\theta = -1$. The fourth-order harmonic has the same value, $\cos 4\theta = 1$, in both directions. Since $I_2(q) > 0$, the spin-flip cross section is therefore larger at $\theta = \{0,\ \pi\}$, producing the field-parallel pair of lobes observed in Fig. 5.

The real-space interval $4 \lesssim \nu_{\mathrm{rms},N} \lesssim 7$ identifies this part of the (f, k) map as a pronounced vortex-profile regime. It is used here as a qualitative reference for interpreting the angular limiting case. Within the fitted linear-vortex representation, the relative radial weight is instead set by $\nu_{\mathrm{rms,fit}}$ and remains q dependent through $[F'(qR)]^2$, which vanishes at $q = 0$ and reaches its maximum near $qR \simeq 2.5$ [23].

b. Parameter region $f = 0$, $0.1 \lesssim k \lesssim 1.0$. In the small-$f$ region, represented here by $f = 0$, Fig. 5 shows a transition from a vertical twofold anisotropy for $k = 0.1$ and 0.25 to a nearly ringlike or weakly horizontal twofold anisotropy for $k \geqslant 0.5$. As shown in Fig. 4, the corresponding orientational moment lies approximately within $0.4 \lesssim \Lambda_N \lesssim 0.8$, while the radial descriptor covers the range $3 \lesssim \nu_{\mathrm{rms},N} \lesssim 7$. The real-space range $3 \lesssim \nu_{\mathrm{rms},N} \lesssim 7$ is used here to characterize the corresponding radial-profile regime. The angular evolution of the fitted linear-vortex representation can then be examined through $\mathcal{A}_1(\theta)$, particularly near the maximum of $|F'(qR)|$ at $qR \simeq 2.5$ [23]. For $\Lambda = 1$,

$$\mathcal{A}_1(\theta, \Lambda = 1) = 3 - \cos 2\theta, \quad (16)$$

which has its maxima at $\theta = \pi/2$ and $3\pi/2$ and therefore exhibits a vertical twofold anisotropy. For $\Lambda = 0$,

$$\mathcal{A}_1(\theta, \Lambda = 0) = 3 + \cos 2\theta, \quad (17)$$

which has its maxima at $\theta = 0$ and π and therefore exhibits a horizontal twofold anisotropy. At the intermediate value $\Lambda = 1/2$,

$$\mathcal{A}_1(\theta, \Lambda = 1/2) = 3, \quad (18)$$

so that $\mathcal{A}_1(\theta)$ is isotropic at this value. Its twofold anisotropy is vertical for $\Lambda > 1/2$ and horizontal for $\Lambda < 1/2$. This interpretation of the transition at $\Lambda = 1/2$ should be understood within the high-ν limit of the reduced vortex model, in which the F'-dependent term governs the angular anisotropy over the relevant finite-q range. This corresponds to the limiting-case analysis used to organize the four characteristic regions of the analytical vortex-SANS landscape in Ref. [24]. For finite values of $\nu_{\mathrm{rms,fit}}$, however, the complete fitted linear-vortex cross section is not generally isotropic at $\Lambda = 1/2$, because the F-dependent angular factor $\mathcal{A}_0(\theta)$ retains second- and fourth-order angular harmonics.

c. Parameter region $0.1 \lesssim f \lesssim 0.4$, $0.1 \lesssim k \lesssim 1.0$. In the intermediate-$f$ region, the orientational moment decreases from moderately positive to negative values and covers approximately $-0.8 \lesssim \Lambda_N \lesssim 0.4$, as shown in Fig. 4. The radial descriptor remains primarily controlled by k and lies within $3 \lesssim \nu_{\mathrm{rms},N} \lesssim 7$. Although Λ_N passes through zero within this region, it remains below $1/2$. Consequently, $\mathcal{A}_1(\theta)$ retains a horizontal twofold anisotropy throughout this part of the parameter grid.

The case $\Lambda = 0$ illustrates why passing through zero does not produce an isotropic spin-flip SANS pattern. In this case, the angular factors reduce to

$$\mathcal{A}_0(\theta, \Lambda = 0) = 4(3 + \cos 2\theta),$$
$$\mathcal{A}_1(\theta, \Lambda = 0) = 3 + \cos 2\theta, \quad (19)$$

and Eq. (5) becomes

$$\left\langle \frac{d\Sigma_{\mathrm{sf}}}{d\Omega} \right\rangle_{\Lambda=0} = I_0(q) + I_2(q)\cos 2\theta, \quad (20)$$

where, for $\Lambda = 0$, the q-dependent intensities are now

$$I_0(q) = \frac{3W}{2}\left[[F(qR)]^2 + \nu_{\mathrm{rms}}^2[F'(qR)]^2\right], \quad (21)$$
$$I_2(q) = \frac{W}{2}\left[[F(qR)]^2 + \nu_{\mathrm{rms}}^2[F'(qR)]^2\right]. \quad (22)$$

An isotropic vortex-axis distribution yields $\Lambda = 0$, although this value is not unique to that distribution. The corresponding cross section nevertheless retains a horizontal twofold anisotropy with maxima at $\theta = 0$ and π. As shown in Fig. 4, Λ_N decreases further toward -1 as f increases, while the principal lobe direction remains field parallel and the angular contrast and fourth-order harmonic change. This explains why the intermediate-f patterns in Fig. 5 can appear similar to the $f \gtrsim 0.5$ patterns despite their different values of Λ_N.

IV. CONCLUSION

Using polycrystalline iron oxide multicore nanoparticles as an example, we have shown how micromagnetic simulations, polarized SANS, and analytical vortex descriptors can be combined in a forward model that maps intraparticle disorder onto collective vortex variables. The nanoflower structures were generated as 3D Voronoi region maps, and the magnetic disorder was varied through two explicit model parameters: the intergrain exchange scale k and the fraction f of grains whose anisotropy axes are aligned with a common reference direction.

The central outcome is that the vortexlike remanent textures are organized by two collective channels. Within the

present forward model, the dominant variation of k is associated with the radial vortex-profile parameter ν_{rms}, whereas the dominant variation of f is associated with the vortex-axis moment $\Lambda = 3\langle\cos^2\alpha\rangle - 1$. The full polar distribution $\psi_\alpha(\alpha)$ remains useful for visualizing the fitted axes, yet its leading projection into the linear-vortex SANS cross section is Λ. Consequently, the micromagnetic parameter space can be interpreted as a mapping of $(k, f) \rightarrow (\nu_{\mathrm{rms}}, \Lambda)$, which positions the simulated nanoflowers in characteristic regions of the analytical vortex-SANS landscape. Here, this micromagnetic mapping refers specifically to the real-space estimators $(\nu_{\mathrm{rms},N}, \Lambda_N)$; the independently fitted SANS parameters quantify how the same textures are represented within the linear-vortex SANS cross section.

This separation is also visible directly in reciprocal space. For weak intergrain exchange, the azimuthally averaged numerical SANS cross section exhibits a pronounced finite-q maximum with $q_{\max}R_{\mathrm{nom}} \simeq 2.5$. With increasing k and decreasing $\nu_{\mathrm{rms},N}$, this maximum shifts toward smaller $q_{\max}R_{\mathrm{nom}}$, while the relative central intensity increases, consistent with a broadening vortex core. In parallel, the variation of Λ_N organizes the transition between vertical twofold, nearly ringlike, and horizontal twofold anisotropies. Independent fits of the linear-vortex model reproduce the normalized numerical SANS morphologies with a mean RMSE of 0.0124. The orientational moments obtained from the SANS and real-space analyses agree closely, whereas the corresponding radial scales exhibit a global nonlinear relation.

The present (k, f) map should therefore be understood as a fixed-size remanent section through a broader vortex-descriptor space. Previous size-dependent nanoflower simulations distinguish core-dominated and flux-closure-dominated reversal regimes [11], whereas the minimal spherical-vortex model demonstrates that the radial profile parameter evolves substantially along the magnetic-field cycle [25]. Particle size, magnetic field, and field protocol may therefore provide additional routes through the same $(\nu_{\mathrm{rms}}, \Lambda)$ descriptor space. The relationships identified here are consequently conditional on the selected particle size and remanent protocol rather than constituting a size-independent classification.

The comparison also clarifies the associated inverse problem. For textures independently identified as vortexlike in real space, the fitted orientational moment Λ_{fit} closely follows the empirical moment Λ_N. This near identity between independently determined quantities provides direct numerical support for Λ as the leading orientational information channel retained by the reduced SANS description. In contrast, the SANS-fitted and real-space radial scales exhibit a global nonlinear relation, so the former should not be interpreted as a direct reconstruction of the latter. Inferring the full vortex-axis distribution or microscopic parameters such as k and f requires additional model information, since similar reduced descriptors may arise from particle size, magnetic field, field protocol, or other structural parameters.

A second level of nonuniqueness concerns the model class itself. Because the real-space ensemble is fully known in the present study, we can trace how its collective information propagates through objectwise vortex fitting, ensemble averaging, Fourier projection, and normalized SANS fitting. This provides a controlled test of the linear-vortex model as a reduced representation, but does not establish that this model can be uniquely identified from SANS data alone. Denoting the normalized fitting residual of a model class schematically by ε, the present result $\varepsilon_{\mathrm{lv}} \ll 1$ does not imply $\varepsilon_{\mathrm{alt}} \gg 1$ for every alternative model class. It demonstrates representability and consistency of the linear-vortex reduction for a known vortex ensemble, but not unique model selection from a normalized SANS cross section.

We propose as a next step to go beyond the leading linear-vortex projection used here. Although the present treatment shows that the leading orientational moment accounts for a large part of the variation in the normalized 2D SANS cross section, the remaining deviations may encode higher-order radial terms and higher spherical moments of the vortex-axis distribution. Such an extension would be conceptually consistent with the second-order power-series analysis introduced previously for the azimuthally averaged magnetic SANS cross section [35]. However, that framework also illustrates the cost of this route: Even for the 1D azimuthal average, the second-order description involves a set of seven intensity coefficients rather than a single additional parameter. A vortex-specific second-order model would therefore have to balance the improved description of the q dependence against a substantially less constrained inverse problem. In this sense, the leading descriptors used here provide the controlled baseline on top of which higher-order corrections can be added.

The model-comparison statements made here refer to individually normalized SANS cross sections. Absolute intensity calibration could provide additional information, but would also introduce further experimental nuisance parameters, including concentration, magnetic volume, saturation magnetization, particle-size dispersion, and instrumental resolution.

ACKNOWLEDGMENTS

M.P.A. acknowledges support by the European Union (Grant Agreement No. 101135546, MaMMoS). J.L. was supported by the Ghent University special research fund (bof/baf/1y/2024/01/005 and bof/baf/1y/2025/01/017). E.M.J. acknowledges funding from the European Union's Horizon 2020 research and innovation program under the Marie Skłodowska-Curie actions (Grant Agreement No. 101081455–YIA, HYPUSH) and from the Institute for Advanced Studies (IAS) of the University of Luxembourg. The computational resources and services used in this work were provided by the HPC facilities of the University of Luxembourg and the Luxembourg National Supercomputer MeluXina. The views and opinions expressed are, however, those of the authors only and do not necessarily reflect those of the European Union or the European Health and Digital Executive Agency (HADEA). Neither the European Union nor the granting authority can be held responsible for them.

DATA AVAILABILITY

The micromagnetic input data, generated nanoflower microstructures, simulation outputs, and analysis scripts associated with this work are available from the Zenodo dataset in Ref. [33].

[1] U. Nowak, O. N. Mryasov, R. Wieser, K. Guslienko, and R. W. Chantrell, Spin dynamics of magnetic nanoparticles: Beyond Brown's theory, Phys. Rev. B **72**, 172410 (2005).

[2] E. M. Jefremovas, L. Gandarias, I. Rodrigo, L. Marcano, C. Gruttner, J. A. Garcia, E. Garayo, I. Orue, A. Garcia-Prieto, A. Muela, M. L. Fernandez-Gubieda, J. Alonso, and L. F. Barquin, Nanoflowers versus magnetosomes: Comparison between two promising candidates for magnetic hyperthermia therapy, IEEE Access **9**, 99552 (2021).

[3] W. Mekseriwattana, N. Silvestri, R. Brescia, E. Tiryaki, J. Barman, F. G. Mohammadzadeh, N. Jarmouni, and T. Pellegrino, Shape-control in microwave-assisted synthesis: A fast route to size-tunable iron oxide nanocubes with benchmark magnetic heat losses, Adv. Funct. Mater. **35**, 2413514 (2025).

[4] J. Borchers, K. Krycka, B. Bosch-Santos, E. de Lima Correa, A. Sharma, H. Carlton, Y. Dang, M. Donahue, C. Grüttner, R. Ivkov, and C. L. Dennis, Magnetic anisotropy dominates over physical and magnetic structure in performance of magnetic nanoflowers, Small Struct. **6**, 2400410 (2025).

[5] A.-H. Lu, E. L. Salabas, and F. Schüth, Magnetic nanoparticles: Synthesis, protection, functionalization, and application, Angew. Chem. Int. Ed. **46**, 1222 (2007).

[6] P. Hugounenq, M. Levy, D. Alloyeau, L. Lartigue, E. Dubois, V. Cabuil, C. Ricolleau, S. Roux, C. Wilhelm, F. Gazeau, and R. Bazzi, Iron oxide monocrystalline nanoflowers for highly efficient magnetic hyperthermia, J. Phys. Chem. C **116**, 15702 (2012).

[7] W. Li, Z. Liang, Z. Lu, X. Tao, K. Liu, H. Yao, and Y. Cui, Magnetic field-controlled lithium polysulfide semiliquid battery with ferrofluidic properties, Nano Lett. **15**, 7394 (2015).

[8] A. Lappas, G. Antonaropoulos, K. Brintakis, M. Vasilakaki, K. N. Trohidou, V. Iannotti, G. Ausanio, A. Kostopoulou, M. Abeykoon, I. K. Robinson, and E. S. Bozin, Vacancy-driven noncubic local structure and magnetic anisotropy tailoring in Fe_xO–$Fe_{3-\delta}O_4$ nanocrystals, Phys. Rev. X **9**, 041044 (2019).

[9] A. Lak, S. Disch, and P. Bender, Embracing defects and disorder in magnetic nanoparticles, Adv. Sci. **8**, 2002682 (2021).

[10] B. G. Prajapati, K. Verma, S. Sharma, and D. U. Kapoor, Transforming cancer detection and treatment with nanoflowers, Med. Oncol. **41**, 295 (2024).

[11] E. M. Jefremovas, L. Calus, and J. Leliaert, Coercivity-size map of magnetic nanoflowers: Spin disorder tunes the vortex reversal mechanism and tailors the hyperthermia sweet spot, Small Sci. **6**, e202500490 (2026).

[12] J. Leliaert and E. M. Jefremovas, Engineering micro-disorder for macro-performance in magnetic nanoparticles, arXiv:2607.28812.

[13] H. Gavilán, A. Gallo-Cordova, M. Rábade-Chediak, A. Páez-Rodríguez, M. d. P. Morales, and L. Gutiérrez, Magnetic hyperthermia in focus: Emerging non-cancer applications of magnetic nanoparticles, Nanoscale **17**, 27734 (2025).

[14] T. Zanette, A. García-Zaragoza, J. Mazarío, J. Santiago Martinez, B. Chaudret, C. Cerezo-Navarrete, and P. Oña-Burgos, Carbon-encapsulated FeNi nanoparticles for efficient magnetically induced levulinic acid hydrogenation, Green Chem. **27**, 11438 (2025).

[15] P. Bender, E. Wetterskog, D. Honecker, J. Fock, C. Frandsen, C. Moerland, L. K. Bogart, O. Posth, W. Szczerba, H. Gavilán, R. Costo, M. T. Fernández-Díaz, D. González-Alonso, L. Fernández Barquín, and C. Johansson, Dipolar-coupled moment correlations in clusters of magnetic nanoparticles, Phys. Rev. B **98**, 224420 (2018).

[16] P. Bender, J. Fock, C. Frandsen, M. F. Hansen, C. Balceris, F. Ludwig, O. Posth, E. Wetterskog, L. K. Bogart, P. Southern, W. Szczerba, L. Zeng, K. Witte, C. Grüttner, F. Westphal, D. Honecker, D. González-Alonso, L. Fernández Barquín, and C. Johansson, Relating magnetic properties and high hyperthermia performance of iron oxide nanoflowers, J. Phys. Chem. C **122**, 3068 (2018).

[17] E. M. Jefremovas, P. Rooms, Á. Gallo-Córdova, M. P. Morales, F. Wiekhorst, A. Michels, and J. Leliaert, Nanoscale mapping of internal magnetization dynamics reveals how disorder shapes heat generation in magnetic particle hyperthermia, Nano Lett. (2026), doi:10.1021/acs.nanolett.6c02907.

[18] S. Mühlbauer, D. Honecker, E. A. Périgo, F. Bergner, S. Disch, A. Heinemann, S. Erokhin, D. Berkov, C. Leighton, M. R. Eskildsen, and A. Michels, Magnetic small-angle neutron scattering, Rev. Mod. Phys. **91**, 015004 (2019).

[19] A. Michels, *Magnetic Small-Angle Neutron Scattering: A Probe for Mesoscale Magnetism Analysis* (Oxford University Press, Oxford, 2021).

[20] P. Bender, D. Honecker, and L. Fernández Barquín, Superferromagnetic correlations in clusters of magnetic nanoflowers, Appl. Phys. Lett. **115**, 132406 (2019).

[21] D. Honecker, L. Fernández Barquín, and P. Bender, Magnetic structure factor of correlated moments in small-angle neutron scattering, Phys. Rev. B **101**, 134401 (2020).

[22] V. Rai, I. Titov, E. M. Jefremovas, v. Liščák, S. Shan, N.-J. Steinke, J. Leliaert, Á. Gallo-Córdova, M. P. Morales, D. Peddis, P. Maltoni, L. F. Barquín, A. Michels, and M. P. Adams, Polarized neutron scattering as a probe for vortex-type spin correlations in iron oxide multicore assemblies, arXiv:2606.18791.

[23] M. P. Adams, E. P. Sinaga, Š. Liščák, and A. Michels, Framework for polarized magnetic neutron scattering from nanoparticle assemblies with vortex-type spin textures, Phys. Rev. B **110**, 014420 (2024).

[24] M. P. Adams, E. M. Jefremovas, and A. Michels, Angular anisotropy landscape of vortex ensembles in polarized small-angle neutron scattering, Phys. Rev. Res. **8**, 023328 (2026).

[25] M. P. Adams and A. Michels, Minimal model for vortex nucleation and reversal in spherical magnetic nanoparticles, Phys. Rev. B **113**, 224406 (2026).

[26] H. Gavilán, A. Kowalski, D. Heinke, A. Sugunan, J. Sommertune, M. Varón, L. K. Bogart, O. Posth, L. Zeng, D. González-Alonso, *et al.*, Colloidal flower-shaped iron oxide nanoparticles: Synthesis strategies and coatings, Part. Part. Syst. Charact. **34**, 1700094 (2017).

[27] H. Gavilán, K. Simeonidis, E. Myrovali, E. Mazarío, O. Chubykalo-Fesenko, R. Chantrell, L. Balcells, M. Angelakeris, M. P. Morales, and D. Serantes, How size, shape and assembly of magnetic nanoparticles give rise to different hyperthermia scenarios, Nanoscale **13**, 15631 (2021).

[28] K. Simeonidis, M. P. Morales, T. Damartzis, N. Maniotis, and S. Veintemillas-Verdaguer, Toward more sustainable magnetic nanoparticle synthesis based on microwave-assisted continuous-flow processes, Ind. Eng. Chem. Res. **63**, 20651 (2024).

[29] A. Vansteenkiste, J. Leliaert, M. Dvornik, M. Helsen, F. Garcia-Sanchez, and B. Van Waeyenberge, The design and verification of MuMax3, AIP Adv. **4**, 107133 (2014).

[30] M. P. Adams and A. Michels, NuMagSANS: A GPU-accelerated open-source software package for the generic computation of nuclear and magnetic small-angle neutron scattering observables of complex systems, J. Appl. Cryst. **59**, 943 (2026).

[31] See Supplemental Material at http://link.aps.org/supplemental/10.1103/mhfg-6sjm for additional information and results supporting this study, which includes Ref. [36].

[32] S. J. R. Holt, A. Petrocchi, M. Lang, S. A. Pathak, and H. Fangohr, Discretization anisotropy in finite difference micromagnetic simulations, IEEE Trans. Magn. **61**, 1 (2025).

[33] M. P. Adams, J. Leliaert, A. Michels, and E. M. Jefremovas, Reduced vortex descriptors linking polycrystallinity in magnetic nanoparticles with polarized magnetic small-angle neutron scattering [Dataset], Zenodo, 2026, https://doi.org/10.5281/zenodo.21322498.

[34] M. P. Adams and A. Michels, Minimal model for vortex nucleation and reversal in spherical magnetic nanoparticles [Dataset], Zenodo, 2026, https://doi.org/10.5281/zenodo.21481863.

[35] M. P. Adams, E. P. Sinaga, H. Kachkachi, and A. Michels, Signature of surface anisotropy in the spin-flip neutron scattering cross section of spherical nanoparticles: Atomistic simulations and analytical theory, Phys. Rev. B **109**, 024429 (2024).

[36] J. Nocedal and S. J. Wright, *Numerical Optimization*, 2nd ed. (Springer, New York, 2006).